Chapter 2

Experimental procedure and characterization techniques

2.1 Sample synthesis

The physical properties of materials are directly linked to their atomic structure at long/short ranges. Moreover, in order to establish a structure-property correlations, synthesized ceramics must undergo comprehensive characterization. This requires the synthesis of high-quality samples. Among various synthesis methods, the solid-state reaction method is one of the most widely used methods, particularly for fabricating perovskite-based ceramics. In the present thesis work, solid-state reaction method has been utilized for sample preparation and to ensure reliable experimental characterizations.

2.1.1 Solid-state reaction method

The solid-state reaction method is a widely used technique for synthesizing polycrystalline or bulk ceramics by using solid precursors as starting reagents [183]. The high-quality precursors are typically oxides and carbonates (see Table 2.1). This method involves a

sequence of mixing/grinding → calcination → sintering → annealing processes, each playing a crucial role in achieving the phase purity and microstructural homogeneity in the synthesized material. The process begins with weighing the precursors (oxides and carbonates; mentioned in Table 2.1) pre-heated at 393 K in an oven as per stoichiometry using a weighing balance (see Fig. 2.1(a)), followed by the mixing of precursors, which can be done using different techniques. One approach involves manually grinding the precursors using an agate mortar and pestle. On the other hand, a more efficient and commonly adopted method is ball milling, which mixes the precursors homogeneously in ethanol media. In the present work, planetary ball mill (Retsch model PM 200) was used (see Fig. 2.1(b)), wherein the weighed precursors were placed in a zirconia jar containing zirconia balls, along with ethanol as a dispersing medium. The milling was carried out for 24 hours in the ball mill at $150 - 200$ rpm. This method facilitates thorough and homogeneous mixing, ensuring a highly uniform precursor mixture or slurry.

Subsequently, the resulting slurry is dried using oven (see Fig. 2.1(c)), and the fine powder is separated from the zirconia balls. The dried powder then undergoes calcination, which is a high-temperature heat treatment process conducted in alumina crucibles using a programmable Muffle Furnace (see Fig. 2.1(e)) capable of reaching temperatures up to 1673 K. During calcination process, the solid-state reactions happen, leading to the formation of the desired crystalline phase by removing volatile impurities. After calcination, the obtained powder is mixed with 2-5 wt% polyvinyl alcohol (PVA), which acts as a binder to improve mechanical integrity during pellet formation. The mixture is then pelletized into disc-shaped samples (having 10 mm or 12 mm thickness) using a hydraulic press (see Fig. 2.1(d)). The final sintering process is performed at a temperature higher than the calcination temperature, further promoting grain growth, densification, and improved microstructural connectivity. Furthermore, the sintered pellets or powder are annealed at certain temperatures using the oven. Once the synthesis is complete, the synthesized

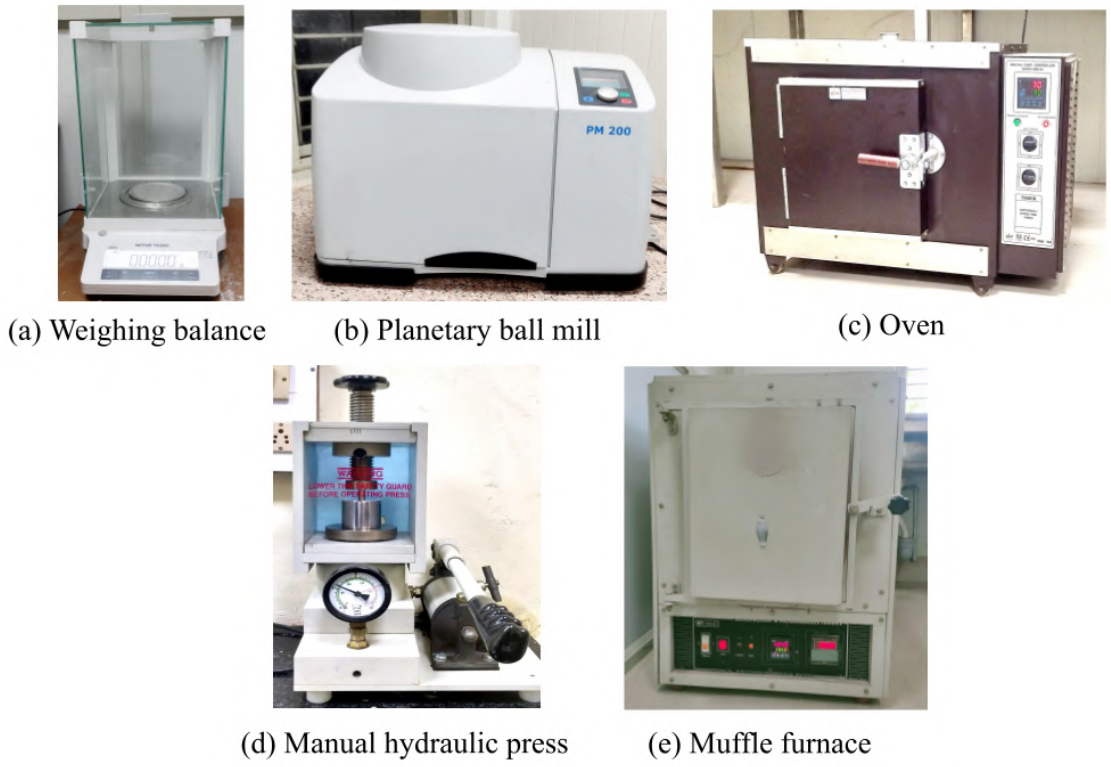

(a) Weighing balance (b) Planetary ball mill (c) Oven

(d) Manual hydraulic press (e) Muffle furnace

Fig. 2.1 Instruments used in the sample synthesis *via* solid-state reaction method.

Table 2.1 Precursors used for sample preparations.

Compositions	Precursors	Company	Assay
$K_xNa_{(1-x)}NbO_3$;	K_2CO_3	Sisco Research Laboratories Pvt. Ltd.	99 %
$0.40 \leq x \leq 0.60$	Na_2CO_3	HIMIDEA LABS	99.5 %
and	$BaCO_3$	HIMIDEA LABS	99 %
$(1\text{-}x)K_{0.5}Na_{0.5}NbO_3\text{-}xBa_{0.9}Sr_{0.1}TiO_3$;	$SrCO_3$	HIMIDEA LABS	99 %
$0.00 \leq x \leq 1.00$	Nb_2O_5	HIMIDEA LABS	99.9 %
	TiO_2	HIMIDEA LABS	99 %

samples are subjected to various structural, dielectric, and ferroelectric characterizations to evaluate their physical properties and confirm phase formation.

2.2 Characterization techniques

In order to explore the structure-property relationship of the synthesized ceramics and to anticipate the materials' potential for different applications, the synthesized ceramics have

been analyzed using the various characterization techniques discussed in the upcoming sections.

2.2.1 X-ray diffraction method

The atomic configuration of any material at various length scales plays a crucial role in tuning its physical properties [8, 184]. X-ray diffraction (XRD) is one of the most powerful and widely used techniques for analyzing the crystal structure of materials. It provides crucial information about the arrangement of atoms in a crystalline solid, resulting in the determination of structural parameters (including lattice parameters and atomic coordinates) and crystal symmetry [185]. When X-rays incident on a crystalline material, they are scattered by the electron clouds of atoms, leading to constructive and destructive interference. The maxima in the intensity occur when a necessary condition (*Bragg's Law*) is satisfied, which is given as:

$$2d_{hkl}sin\theta = \lambda \tag{2.1}$$

Here, d_{hkl} corresponds to the interplanar spacing, λ is the wavelength of the X-ray source, and θ corresponds to the Bragg's angle *i.e.*, the angle between the incident ray and the plane, thereby 2θ becomes the angle between the incident and the diffracted beam (see Fig. 2.2). The diffraction pattern carries intrinsic information about the crystallographic structure, which can be analyzed to determine structural parameters [186, 187].

Moreover, in order to determine the purity, structural configurations, and related structural parameters of the synthesized ceramics, X-ray diffraction measurements are performed. Various X-ray diffraction measurements on different setups have been performed to analyze the structural configurations of synthesized ceramics. Firstly, we performed X-ray measurements using an in-house Rigaku Miniflex 600 Desktop X-Ray Diffraction System (600 W) having Cu Kα_1 and Kα_2 radiation source, operated in Bragg–Brentano

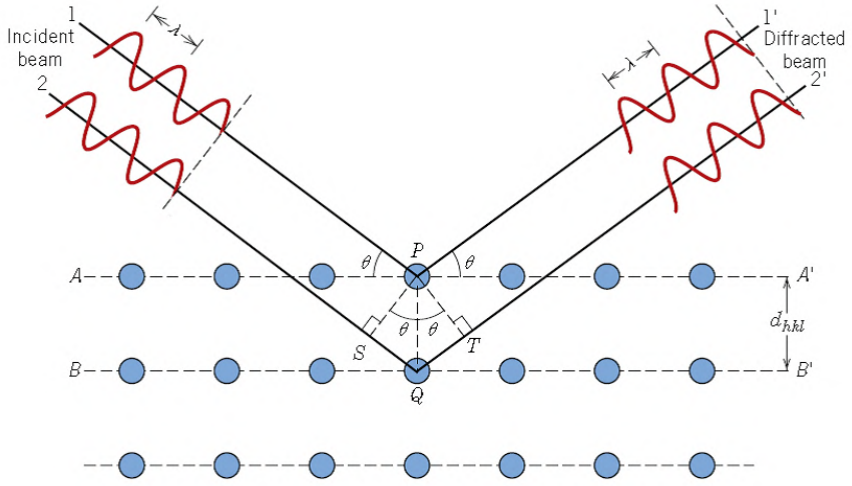

Fig. 2.2 Schematic representation of X-ray diffraction in a crystal.

geometry (see Fig. 2.3(a)). Secondly, a high-resolution X-ray diffraction measurement has been performed using an in-house Rigaku SmartLab 9kW system with a monochromatic source Cu Kα_1 radiation (see Fig. 2.3(b)). The X-ray diffraction data have been collected over the 2θ range from 20^0 to 120^0 with a step size of 0.02. The data were recorded in a continuous scan mode. Further, high-energy diffraction data have been obtained from different synchrotron X-ray sources at different wavelengths available at Argonne National Lab ($\lambda \approx 0.1173$ Å) and Brookhaven National Lab ($\lambda \approx 0.1821$ Å and ≈ 0.1665 Å). Furthermore, in order to fix the crystallographic structure of the various synthesized ceramics, we have performed the Le Bail and Rietveld refinements of the X-ray diffraction data using the FULLPROF package [188].

2.2.2 Neutron diffraction method

The X-ray diffraction (XRD) technique depends on the scattering of electromagnetic waves by the electron cloud surrounding atoms, making it highly sensitive to elements with high atomic numbers (Z). However, X-rays are less effective in distinguishing light

Fig. 2.3 (a) Bench-top XRD and (b) HR-XRD used for diffraction measurements.

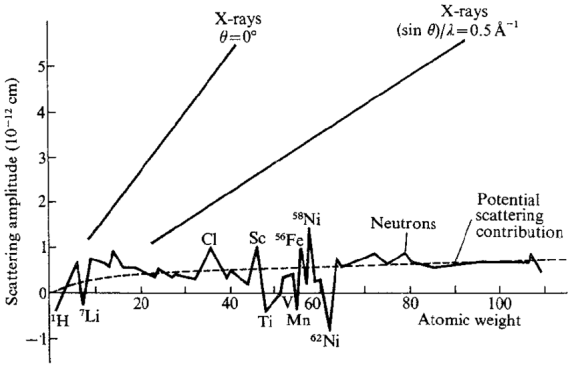

Fig. 2.4 X-ray vs Neutron scattering amplitudes.

elements such as hydrogen, lithium, or oxygen when they coexist with heavier elements due to their weak scattering power. Thus, for precise determination of structural parameters involving low Z atoms, neutron diffraction is used instead of X-ray diffraction. Neutron diffraction uses neutrons, which interact directly with the atomic nuclei rather than the electron cloud. This fundamental difference allows neutron diffraction to be equally sensitive to both light and heavy elements, making it particularly advantageous for studying hydrogen/oxygen/lithium-containing materials and magnetic structures (see Fig.

2.4). In the present study, neutron diffraction measurements were performed at the D1B diffractometer at Institut Laue-Langevin (ILL), Grenoble (λ = 1.28 Å).

Rietveld refinement

Rietveld refinement is a powerful and widely used technique for structural analysis of materials using diffraction data obtained after X-ray/neutron diffraction measurements. It is based on the fundamental principle of optimizing crystal structures by refining the intensities and positions of diffraction peaks to achieve the best fit between the observed and calculated patterns [189, 190]. The Rietveld refinements result in the determination of structural parameters, which include lattice parameters (a, b, c, α, β, and γ), atomic coordinates (x, y, and z), and thermal vibrations (isotropic/anisotropic). Additionally, various authors used the Rietveld method to probe local off-centered displacements present in the materials exhibiting an average cubic structure [191, 192].

The Rietveld method uses a structural model to fit the observed diffraction pattern, and if the model closely corresponds to the real structure, it generates intensity values (calculated intensity) that align with the experimental data. The core principle of the Rietveld algorithm is to iteratively optimize the model function by minimizing the difference between observed and calculated intensities, quantified by the function *viz.*, Σ_i $w_i[y_i(obs)\text{-}y_i(calc)]^2$ [189, 190]. Here, y_i(obs) is the measured intensity at step i, y_i(calc) is the calculated intensity, and w_i represents the weighting factor, often defined as $\frac{1}{y_i(obs)}$. The calculated intensity is derived from analytical functions (corresponding to the given structural model), incorporating various structural and profile parameters, such as atomic positions, lattice parameters, site occupancies, peak shape and width, background correction, sample displacement, zero-shift error, preferred orientation, etc. These parameters are refined using the least-squares method to achieve the best agreement between the observed and simulated (or calculated) diffraction profiles [189, 190]. Since the refinement process

involves various adjustable parameters, it can sometimes converge to false minima or even diverge. In order to avoid such issues, the initial structural model should be as close as possible to the actual crystal structure. Moreover, proper background modeling using appropriate mathematical functions and high-quality diffraction data significantly improves refinement accuracy. During the refinement cycles, it is essential to visually monitor the fitting process at each step to ensure that refinement progresses correctly, and finally achieve an optimal match between the experimental and calculated diffraction patterns [189, 190]. Further, to ensure the goodness of fit between the observed and calculated pattern, various agreement factors or *R* values were described as:

$$R_{wp} = \left\{ \frac{\sum_i w_i [y_i(\text{obs}) - \text{y}_\text{i}(\text{calc})]^2}{\sum_i w_i [y_i(\text{obs})]^2} \right\}^{1/2} \tag{2.2}$$

$$R_{exp} = \left\{ \frac{N-P}{\sum_i^N w_i y_i(\text{obs})^2} \right\}^{1/2} \tag{2.3}$$

Here, N and P correspond to the number of data points and the number of parameters, respectively. Generally, the quality of the fit between the observed and calculated diffraction patterns is often evaluated using these statistical parameters. One of the key parameters is the weighted profile R-factor (R_{wp}), which is ideally expected to be close to the expected R-factor (R_{exp}) for a good refinement. Another commonly used metric is the goodness-of-fit parameter (χ^2), which is mathematically defined as:

$$\chi^2 = \left(\frac{R_{wp}}{R_{exp}} \right)^2 \tag{2.4}$$

For a good refinement, χ^2 should ideally approach 1, indicating that the model accurately describes the experimental data [193]. However, while these statistical indicators provide useful insight into the refinement process, they should not be over-interpreted. A low χ^2 value does not always guarantee a good fit, as it may be influenced by factors such

as peak broadening, preferred orientation, or instrumental errors. The most reliable way to assess the quality of a Rietveld refinement is by carefully examining the visual agreement between the observed and calculated diffraction profiles, particularly by analyzing the difference plot [193, 194].

2.2.3 Microstructure measurement

Fig. 2.5 BT-SEM used for microstructural analysis.

The ferroelectric properties of perovskite materials are strongly influenced by their grain structure. The presence of grains often leads to discontinuities in spontaneous polarization at the grain boundaries, which in turn induce a depolarizing field. Simultaneously, the polarization also causes lattice distortion (or structural deformation), which generates internal stress fields at grain boundaries. In order to minimize electrostatic energy (from depolarization field) and mechanical strain energy (from internal stress field), the system stabilizes through the formation of smaller regions known as ferroelectric domains, which exhibit complex patterns and unique behaviors [195]. The polarization within a domain aligns according to the symmetry of the material, and adjacent domains are separated

by domain walls, which typically range from 1 nm -10 nm [196]. When an external electric field is applied in a direction that is not parallel to the domain walls, it induces domain wall motion. On a microscopic level, this results in polarization switching near the domain walls, leading to growth or shrinkage of domains depending on the field direction [197]. This dynamic process contributes to the extrinsic effects in dielectric and piezoelectric properties, demonstrating how microstructural characteristics are crucial in determining the material's overall physical properties [197]. In this thesis work, the microstructural observations were performed using a scanning electron microscope (JCM-6000 Plus BenchTop SEM Neoscope) (see Fig. 2.5) to determine homogeneity and grain size.

2.2.4 Dielectric measurements

Dielectric materials are essentially insulating materials that can be polarized when subjected to an external electric field. The polarization occurs due to the rearrangement of charges within the material. When an electric field is applied, positive charges shift in the direction of the field, while negative charges move in the opposite direction. The strength of the polarization depends on the dielectric constant of the material. Based on their response to an external electric field, dielectric materials are broadly classified into linear and non-linear dielectrics. Linear dielectrics exhibit a direct proportionality between polarization and the applied field. On the other hand, non-linear dielectrics (such as ferroelectrics, relaxors, and anti-ferroelectrics) exhibit a more complex polarization behavior, often characterized by hysteresis loops, making them useful in sensors, actuators, energy harvesters, and memory devices [198, 199]. As discussed above, the polarization varies linearly for linear dielectrics, which is given as: [198, 199]

$$P = \varepsilon_0 E \chi \tag{2.5}$$

$$\chi = \varepsilon_r - 1 \tag{2.6}$$

Here, P corresponds to the polarization of the dielectric material, ε_0 (= 8.854×10^{-12} F/m) is the permittivity of the free space, E is the applied electric field, χ is the electric susceptibility, and ε_r is the relative permittivity ($\varepsilon_r = \varepsilon/\varepsilon_0$) [199].

On the other hand, for non-linear dielectrics (polarization does not vary linearly), when the applied electric field increases, polarization rises to a maximum value (P_{max}). However, on decreasing the field, polarization decreases but does not return to zero; instead, a remnant polarization (P_r) persists even when the field is removed. Further, on increasing the magnitude of the field in the opposite direction, the polarization vanishes at a certain field referred to as the coercive field (E_C). The complete cycle repeats itself and demonstrates hysteresis [198, 200]. Moreover, non-linear dielectric materials such as ferroelectrics, antiferroelectrics, relaxor ferroelectrics, and relaxor antiferroelectrics possess unique electrical properties, making them highly valuable for applications in energy storage, sensors, actuators, and capacitors [198, 199]. Further, when an alternating electric field is applied, polarization continuously switches direction in response. However, at high frequencies, a phase lag occurs between the applied field and the dipole alignment, which is observed in the electric field vector (E) & the electric displacement vector (D) and is given as:

$$E = E_0 e^{i\omega t} \tag{2.7}$$

$$D = D_0 e^{i(\omega t - \delta)} \tag{2.8}$$

Here, E_0 is the amplitude of the electric field vector (E), and D_0 is the amplitude of the electric displacement vector (D).

According to the equation

$$D = \varepsilon E \tag{2.9}$$

$$D_0 e^{i(\omega t-\delta)} = \varepsilon^* \varepsilon_0 E_0 e^{i\omega t} \tag{2.10}$$

Here, ε^* represents the complex dielectric permittivity given as

$$\varepsilon^* = \varepsilon' - i\varepsilon'' \tag{2.11}$$

ε' and ε'' corresponds to the real and imaginary part of dielectric permittivity. The imaginary part, *i.e.,* ε'' also corresponds to the dielectric loss of the materials. Thus using equations (2.10) and (2.11), ε' and ε'' can be expressed as

$$\varepsilon' = \frac{D_0}{\varepsilon_0 E_0}\cos\delta \tag{2.12}$$

and

$$\varepsilon'' = \frac{D_0}{\varepsilon_0 E_0}\sin\delta \tag{2.13}$$

these two equations give rise to

$$\tan\delta = \frac{\varepsilon''}{\varepsilon'} \tag{2.14}$$

Fig. 2.6 Keysight LCR meter used for dielectric measurements.

Here, the quantity $\tan\delta$, *i.e.,* loss tangent (dissipation factor). In the thesis work, we have prepared various pellets of different samples with good electrical contact (using silver paste) and performed the temperature-dependent dielectric measurement at various frequencies using Keysight LCR meter (see Fig. 2.6) with a heating rate 1-2 ^{0}C/min.

2.2.5 Ferroelectric characterization (P-E loop measurements)

The non-linear dielectric materials exhibit polarization (total dipole moment per unit volume) in response to an applied external electric field (E_{ext}). This induced polarization generates an internal electric field (E_{ind}) that opposes the applied external field. Consequently, the net electric field within the dielectric material is given by:

$$E_{net} = E_{ext} - E_{ind} \tag{2.15}$$

This reduction in the net electric field lowers the voltage across the dielectric, thereby enhancing its capacitance ($C = \frac{Q}{V}$), which is a critical factor for energy storage applications. The ability of dielectric materials to store and release energy is commonly assessed through polarization vs. electric field (P-E) hysteresis loop measurements. Unlike linear dielectrics, which exhibit a direct relationship between polarization and the applied field (see Fig. 2.7(a)), non-linear dielectrics display characteristic hysteresis loops based on their material properties. Different types of dielectric materials exhibit distinct P-E loops. Ferroelectric materials are characterized by a S-shaped hysteresis loop, indicative of their strong remnant polarization (see Fig. 2.7(b)). In contrast, relaxor ferroelectrics exhibit a slim P-E loop (see Fig. 2.7(c)). Moreover, antiferroelectric materials exhibit a double hysteresis loop (see Fig. 2.7(d)), and the relaxor antiferroelectrics exhibit a slim double hysteresis loop due to their structural disorder. In this thesis work, P-E loops were recorded using Radiant Technology's Precision LC II Ferroelectric tester to gain insights into the electric properties of the synthesized materials (see Fig. 2.8).

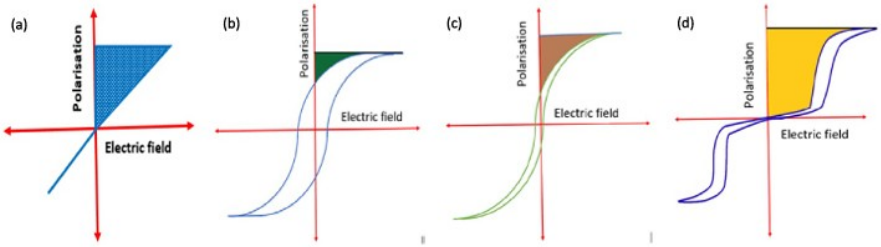

Fig. 2.7 Different shapes of P-E loops.

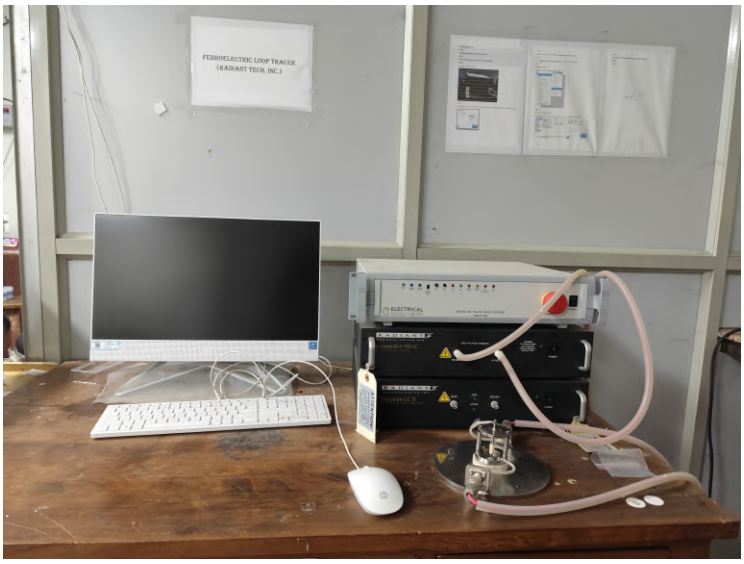

Fig. 2.8 Polarization *vs.* electric field (P-E) loop tracer by Radiant technologies.

2.2.6 Raman spectroscopic measurements

Raman spectroscopy is a powerful technique based on the interaction of electromagnetic wave (generally visible region) with matter, specifically through the inelastic scattering of photons [201, 202]. Raman scattering probes the internal vibrations of BO_6 octahedra of ABO_3 perovskites. Traditionally, X-ray diffraction probes the average structure (atomic order at long ranges) and cannot probe the short range order, which gives a reason to Raman spectroscopy [201, 202]. Moreover, it is well known that X-ray diffraction probes an average structure up to a few hundreds of angstroms ($\approx$ 100 Å), whereas Raman spectroscopy probes the atomic structure up to a few tens of angstroms ($\approx$ 30 Å$-$ 40 Å) [203].

Further, when a monochromatic light interacts with the material, the electromagnetic field disturbs the charge distribution within the molecules, leading to an exchange of energy and momentum. This interaction can result in two types of scattering *viz.*, elastic (Rayleigh scattering), where there is no energy difference between the incident and scattered photons (*i.e.*, incident photon retains its energy), and inelastic scattering (Raman scattering), where the photon either gains or loses energy [201, 202]. The latter phenomenon is referred to as the Raman effect, which was first experimentally observed in 1928 by Sir C. V. Raman, earning him the Nobel Prize in Physics in 1930. In the Raman effect, when a photon interacts with a material, it results in excitation of a vibrational mode within the lattice, thereby causing a shift in the energy of the photon. If the scattered photon loses energy, it produces a Stokes shift, whereas if it gains energy, it results in an anti-Stokes shift. These shifts provide information about the vibrational states of the material, which are directly linked to its structure (at long/short ranges) and associated properties [201, 202]. For crystalline materials, this energy transfer excites quantized lattice vibrations known as phonons, making Raman spectroscopy particularly useful for studying structural phase transitions, lattice dynamics, and other related phenomena. As discussed above, during the Raman scattering process, the energy of the scattered light undergoes a shift due to its interaction with the phonons. The relationship governing this frequency shift is given as:

$$\omega_{scat} = \omega_p \pm \omega_{osc} \tag{2.16}$$

Here, ω_{scat}, ω_{p}, and ω_{osc} is the frequency of the scattered photon, frequency of the incident photon, and lattice vibrational frequency (phonon mode), respectively. Apart from energy conservation, momentum is also conserved in the Raman scattering process, which is given as:

$$\overrightarrow{k}_{scat} = \overrightarrow{k}_{p} \pm \overrightarrow{k}_{q} \tag{2.17}$$

where $\overrightarrow{k}_{scat}$ and $\overrightarrow{k}_{p}$ are the wave vectors of the scattered and incident photons, respectively, while $\overrightarrow{k}_{q}$ represents the wave vector of the phonon (lattice vibration).

Now, when molecules/crystals are subjected to an externally applied field, their charge distribution undergoes a perturbation. However, this perturbation occurs in accordance with the intrinsic symmetry of the crystal, leading to the formation of dipoles, which can exhibit anisotropic behavior. This anisotropic behavior is described as polarizability in molecules and dielectric susceptibility in crystals. According to classical theories, the Raman effect arises due to variations in polarizability (for molecular vibrations) or changes in dielectric susceptibility (for lattice vibrations in crystals), both of which originate from the vibrations of interatomic bonds within the material [204].

Furthermore, the Raman spectrum consists of several peaks that are associated with vibrations of interatomic bonds, creating a unique spectral fingerprint for each material. This distinct spectral fingerprint allows Raman spectroscopy to be a powerful tool for crystal structure analysis, which results in identification of complex crystal phases driven by octahedral rotations, cationic polar displacements, and other octahedral distortions [21, 104, 205, 206, 207]. Moreover, Raman peaks provide crucial insights into a material's structural and vibrational properties *via* three main parameters *viz.*, peak position, peak width, and peak intensity [202]. Firstly, the peak position represents the vibrational frequency (or vibrational energy) of the particular vibrational mode, which shifts due to strain, temperature, or structural phase transitions. Secondly, the peak width describes the crystal disorder. Similar to X-ray diffraction, sharp Raman peaks indicate crystalline samples while broad Raman peaks indicate amorphous samples [202]. Finally, the peak intensity depends on the polarizability of the particular vibrational mode, thereby giving information of ferroelectric/polar content in the material [202]. These parameters make Raman spectroscopy a vital tool for analyzing material properties and associated structural phase transitions [202].

In this thesis work, we have used the Raman spectroscopy technique to probe the long/short-range symmetries of the synthesized ceramics. The room-temperature Raman spectra was obtained using the alpha300 RAS system from WITec with an excitation source of 532 nm green laser (see Fig. 2.9). Moreover, the temperature-dependent Raman spectra were acquired using a Horiba LabRAM HR Raman spectrometer with an Olympus BX41 microscope attachment. An excitation wavelength of 514.5 nm from a Lexel Model-95 argon ion laser was used. The samples were placed in a Linkam THMS600 microscope stage for variable temperature Raman measurements. The laser beam was focused onto the sample using a 50x LWD objective (N.A.= 0.50), and the backscattered light was dispersed *via* a 600 lines/mm grating onto a liquid nitrogen cooled CCD detector. The data was acquired using LabSpec v5 software. Laser power at the sample was approximately 0.4 mW. This value was checked to verify that no local heating effects from the laser beam occurred.

Fig. 2.9 Raman Instrument used for room temperature measurements.

2.2.7 Pair Distribution Function method

The Pair Distribution Function (PDF) method is a powerful technique used to investigate the atomic ordering of materials at various length scales. Unlike conventional crystallographic methods that rely solely on Bragg diffraction peaks, the PDF method utilizes total scattering data, incorporating both Bragg and diffuse scattering contributions [208, 209, 210]. Moreover, PDF provides information regarding atomic order at short- and intermediate ranges, making it suitable for studying materials with complex atomic arrangements, such as nanoparticles, glasses, disordered crystals, etc [208, 209, 210]. The Pair Distribution Function (PDF) is derived from total scattering experiments using high energy X-ray/neutron diffraction techniques. The process begins with collecting high-energy diffraction data in reciprocal space. The total intensity (I_T) of the scattered X-ray/neutron beam is given as [209]:

$$I_T = I_C + I_{IC} + I_{MC} + I_{BG} \tag{2.18}$$

where, I_C, I_{IC}, I_{MC}, and I_{BG} correspond to the coherent part of intensity, incoherent part of intensity, multiple scattering intensity, and background intensity, respectively. Here, it is important to mention that the background intensity mentioned here corresponds to the scattering intensity without the sample, due to air, and other instrumental parts [209]. The total scattering intensity is measured as a function of scattering angle 2θ and wavelength λ. The scattering angle 2θ and wavelength λ are related to each other *via* diffraction vector (or momentum transfer vector) Q, which is given as [208, 209]:

$$|Q| = \frac{4\pi sin\theta}{\lambda} \tag{2.19}$$

The maximum Q value can be obtained at $\sin\theta = 1$ *i.e.*, $Q = 4\pi/\lambda$. Common laboratory X-ray sources, such as Cu K_α radiation with a wavelength of 1.54 Å, provides a maximum

accessible Q-range of ≈ 8 Å^{-1} [209]. However, this Q-range is insufficient for high-quality PDF analysis, because accurate real-space structural information requires a broader Q-range. In order to obtain reliable PDF data, high-energy (low-wavelength) X-rays or neutrons are needed, thereby resulting in large Q_{max} values [208, 209, 210]. The total intensity is corrected to exhibit only coherent part (I_C) by subtracting other contributions (I_{IC}, I_{MC}, and I_{BG}) which do not contain any structural information. Subsequently, the corrected intensity (I_C or I_{coh}) obtained from the high-energy SXRD data is reduced to total scattering structure function S(Q), which is given as [208, 211]:

$$S(Q) = 1 + \frac{[I_{\text{coh}}(Q) - \sum c_i |f_i(Q)|^2]}{|\sum f_i(Q) c_i|^2} \tag{2.20}$$

Here, I_C/I_{coh} is the corrected/coherent part of intensity, c_i, and f_i(Q) correspond to atomic concentrations and X-ray structure factor of i^{th} atomic species [208, 209, 211]. Further, the obtained S(Q) is transformed to the final pair distribution function [G(r)] using Fourier transformation given as [118, 208, 209, 211, 212]:

$$G(r) = \frac{2}{\pi} \int_{Q_{\text{min}}}^{Q_{\text{max}}} Q[S(Q) - 1] sin(Qr) dQ \tag{2.21}$$

The G(r) pattern obtained from pair distribution function (PDF) analysis represents the distribution of atomic pair distances within a material. The PDF profile exhibits multiple peaks, and important structural information can be extracted by analyzing the peak characteristics *viz.*, peak position, peak intensity, and peak width. Firstly, the peak position directly corresponds to the atomic bond lengths in the material. Secondly, the peak intensity corresponds to the coordination number of that particular pair of atoms, and lastly, the peak width (or peak shape) corresponds to the atomic probability distribution. Further, various structural models are used to fit the G(r) patterns using PDFGUI software [213].

In the present thesis work, we have obtained high-energy X-ray diffraction data from two different sources *viz.*, Argonne National Lab with λ = 0.1173 Å (Q_{max} = 28 $Å^{-1}$) and Brookhaven National Lab with λ = 0.1821 Å (Q_{max} = 18.1 $Å^{-1}$ and 23.6 $Å^{-1}$) and λ = 0.1665 Å (Q_{max} = 27.8 $Å^{-1}$).